ELSEVIER

Journal of Chromatography A, 805 (1998) 149–160

JOURNAL OF CHROMATOGRAPHY A

Numerical simulation of band-broadening during hydrodynamic relaxation in frit-inlet field-flow fractionation channels

Jean-Claude Vauthier, P. Stephen Williams*

Field-Flow Fractionation Research Center, Department of Chemistry, University of Utah, Salt Lake City, UT 84112, USA

Received 26 August 1997; received in revised form 9 December 1997; accepted 30 December 1997

Abstract

The frit-inlet technique is a promising implementation of hydrodynamic relaxation of samples in field-flow fractionation (FFF). The optimization of the process is of great importance in order to maximize overall system efficiency. The mechanism of band-broadening that takes place during hydrodynamic relaxation has been examined using a three-dimensional simulation of the flow inside the triangular end-piece of the channel. This is the first time this contribution to band-broadening has been considered and studied. Particle trajectories in the absence of a transverse field were numerically calculated, thereby isolating this effect from the familiar field-driven relaxation effect. As a first step towards an optimization of the system, the influence of the length of frit element was examined. Band-broadening was examined by determining the number of particles passing through the triangular end-piece as a function of transit time for a uniform particle distribution at the injection point. Due to the complexity of the flow patterns within the system, it is concluded that such numerical simulations are necessary for the optimization of the design and operation of this type of channel. © 1998 Elsevier Science B.V.

Keywords: Field-flow fractionation; Band broadening; Hydrodynamic relaxation; Frit-inlet technique

1. Introduction

Field-flow fractionation (FFF) comprises a family of separation techniques suitable for analyzing polymers, colloids and larger particles ranging from about 1 μm to 100 μm in diameter [1–5]. The separation is carried out within a flow of fluid driven through a thin, parallel-walled channel. The thin geometry of the channel gives rise to a parabolic fluid velocity profile between the parallel walls, with small perturbations close to the edge walls. A field is applied across the thin dimension, perpendicular to the direction of fluid flow, to drive the sample components (i.e., the different molecules or particles comprising the sample) towards one of the parallel channel walls. Consequently, there is a build-up of concentration close to this wall, the so-called 'accumulation wall', and a reduction near the opposite wall, which is referred to as the 'depletion wall'. The (possibly) differing rates of migration toward the accumulation wall opposed by differing rates of back-diffusion or, in the case of larger components, differing strengths of hydrodynamic lift force (which tend to drive materials away from the walls, see for example Ref. [6]) lead to differing concentration profiles across the channel thickness for the different components of the sample. The different distributions of the components within the parabolic fluid

*Corresponding author.

0021-9673/98/$19.00
PII S0021-9673(98)00009-0

velocity profile result in their having different migration velocities along the length of the channel. Different components therefore emerge at the channel outlet at different times and separation is thereby achieved.

The sample is generally introduced to the channel inlet as a small plug of solution or suspension. In the case of a conventional channel inlet which does not make use of hydrodynamic relaxation, the sample components may be assumed to be initially distributed quite uniformly across the channel thickness. Commonly, the channel flow is halted for a short period following sample introduction to allow the sample components to approach their final distributions under the influence of the transverse field [7]. This is known as the stop-flow procedure for sample relaxation. The flow is subsequently restarted to carry out the separation. If the sample components are allowed to relax toward their respective distributions across the channel thickness without interrupting the flow, a considerable spreading of the materials along the length of the channel occurs [8], with consequent loss of separation efficiency. An alternative to the stop-flow method of sample relaxation is a technique known as hydrodynamic relaxation, an implementation of which is the topic of interest here.

The concept of hydrodynamic relaxation of sample near the inlet of a field-flow fractionation channel was introduced by Giddings [9]. Two different designs of channel inlet have been proposed to implement the technique: the split inlet [10] and the frit inlet [11]. In both cases the channel inflow is derived from two substream sources, namely, the sample inlet-flow, into which the small plug of sample is introduced, and a complementary carrier fluid-flow. In the case of the split inlet, the substreams enter the channel on either side of a physical stream splitter that is generally placed mid-way between, and must be parallel to the accumulation and depletion walls. The sample inlet-flow enters the channel adjacent to the accumulation wall while the complementary carrier-flow enters adjacent to the depletion wall. In the case of the frit inlet, the sample inlet-flow enters at the conventional channel inlet close to the tip of the triangular end-piece, and the complementary carrier-flow enters through a short piece of porous frit material incorporated into the

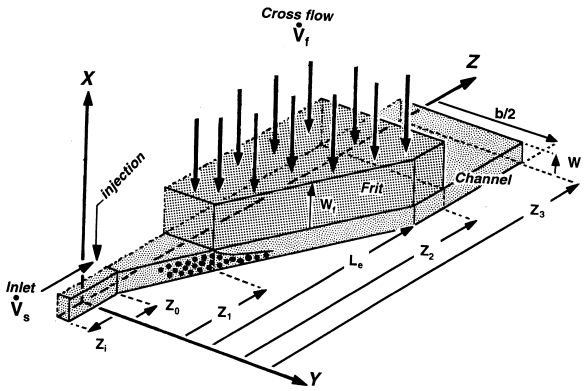

Fig. 1. Geometry of the computational domain.

depletion wall of the channel, just downstream of the sample entry port (see Fig. 1). In either design, the sample components are driven toward the accumulation wall by the diversion of the sample substream on merging with the, generally higher, complementary substream. Ideally, the merging of substreams confines the sample components to a thin fluid lamina adjacent to the accumulation wall. Following this hydrodynamic relaxation step, a small amount of additional field-driven relaxation is necessary for each component to approach its final steady-state distribution. This takes place under elution conditions and takes care of under or over-relaxation of different components, and the redistribution of each component into its steady-state concentration profile. When hydrodynamic relaxation results in a thin sample lamina, the residual field-driven relaxation of the sample components toward their steady-state distributions occurs relatively quickly because of the greatly reduced distances over which this transport of materials takes place. The band-broadening associated with this residual field-driven relaxation is greatly reduced by the preceding hydrodynamic relaxation. This is because the sample components are brought close to their final steady-state distributions adjacent to the accumulation wall, and more importantly, sample materials do not therefore pass through the fast-flowing streamlines around the central regions of the channel thickness during the field-driven relaxation step.

By eliminating the need for a stop-flow procedure, the technique of hydrodynamic relaxation provides

for rapid separation [10,12–14]. It also has the advantages of avoiding baseline instabilities associated with valve switching, and reducing the tendency for particle adhesion to the accumulation wall that may occur with the stop-flow procedure. However, unavoidable incremental band-broadening effects are associated with the hydrodynamic relaxation process [12], and it is important to minimize these contributions to band-broadening in order to maximize the overall system efficiency. The efficiency of a split- or frit-inlet system is dependent in part upon the thickness x_s of the hydrodynamically relaxed sample lamina. As mentioned above, a thin sample lamina following hydrodynamic relaxation is conducive to rapid residual relaxation. If we ignore the complications to flow associated with the geometry of the triangular end-piece and assume that all streamlines have zero velocity components in the Y direction, then, for an otherwise ideal system, we would expect x_s to be constant across the channel breadth. In this case the ratio of x_s to channel thickness w is related to the ratio of sample-inlet flow-rate $\dot{V}_s$ to total channel flow-rate $\dot{V}$ according to the equation [15]:

$$\frac{x_s}{w} = \sin(\theta/3) + 0.5 \quad (1)$$

where

$$\sin\theta = 2(\dot{V}_s/\dot{V}) - 1 \quad (2)$$

and where θ is confined to the range $-\pi/2 \leq \theta \leq \pi/2$. A small ratio $\dot{V}_s/\dot{V}$ is therefore required to facilitate hydrodynamic sample relaxation. However, as pointed out by Giddings [11], while a reduced sample inlet flow-rate $\dot{V}_s$ improves hydrodynamic relaxation, it amplifies the contribution to sample zone breadth due to finite sample volume. This is because a given sample volume requires a longer time for introduction at a reduced flow-rate $\dot{V}_s$. At the same time, any band-broadening which occurs as the sample is swept through the inlet tubing and other inlet dead volumes is amplified. A certain amount of band-broadening also arises out of the differing path lengths and velocities of streamlines through the triangular inlet end-piece [16,17]. In the case of a split inlet where the stream splitter extends beyond the end-piece, this band-broadening may also be expected to be amplified to a similar degree. The situation with regard to this latter effect is more complicated in the case of a frit inlet because of the frit inflow that generally occurs throughout a major part of the end-piece. Nevertheless, we can assume that this effect would be amplified to some degree.

The experimental flow-rates $\dot{V}_s$ and $\dot{V}$ must be chosen such that overall band-broadening is minimized. Since the processes described are independent of one another, their contributions to band-broadening, expressed in terms of plate height, are simply additive. As the ratio $\dot{V}_s/\dot{V}$ is reduced the contribution to plate height due to residual relaxation H_r decreases, while the contributions due to finite sample feed volume H_f, flow through inlet dead volumes H_{di}, and triangular end-piece effects H_e all increase. The determination of optimum $\dot{V}_s/\dot{V}$ ratio corresponding to a minimized sum of $H_r + H_f + H_{di}$ has been dealt with previously [12]. (Note that in this treatment $H_f + H_{di}$ was referred to as H_{end}, and the contribution H_e, as defined here and in Refs. [16] and [17], was ignored). Nevertheless, the approach presented is expected to be quite acceptable for split-inlet systems. However, in the case of the frit-inlet system, there are additional contributions to plate height, besides H_e, which have not been considered to date, and these will be collectively referred to as H_{frit}. Within the frit inlet, a form of relaxation band-spreading takes place as those particles or macromolecules that are initially located close to the depletion wall are driven toward the accumulation wall, not by the influence of the field but by the merging of the two carrier fluid streams. As they are driven across the central regions of the channel thickness they encounter more quickly flowing streamlines and are carried ahead of those particles or macromolecules that enter the channel close to the accumulation wall. This effect results in the major contribution to H_{frit}. In the split-inlet system this effect is negligible. Here, the sample initially occupies a region adjacent to the accumulation wall having a thickness that is, at most, equal to $w/2$. The sample is then expected to be hydrodynamically relaxed within a distance comparable to the channel thickness. The particles or macromolecules are therefore quickly driven away from the central regions of the channel thickness. They are displaced from the central regions before the fully developed parabolic fluid velocity profile is obtained. There is compara-

tively little time and little tendency for differential displacement along the separation axis.

For the complicated geometry of a triangular end-piece with complementary inflow via a frit element that is partially or entirely included in the triangular region, we cannot expect x_s to be constant across the channel breadth. We expect small contributions to H_{frit} to result from this effect. The length and shape of the frit element will influence this variation of x_s and are parameters that should therefore be optimized in the design of the separation cell. Various configurations have been proposed by Giddings [11], but the influence of such geometric parameters on band-broadening is at present unknown. The first steps in examining the influence of frit element length on the flow patterns are taken here.

The contribution to band-broadening due to hydrodynamic relaxation within the region of a frit inlet is the subject of the present study. The approach involves a three-dimensional modelling of the flow pattern through the triangular end-piece and a short section of the channel near the inlet. The band-broadening determinations therefore reflect the combined effects of both H_{frit} and H_e. The study is restricted to the theoretical analysis of the process of hydrodynamic relaxation of micron-size particles in the region of a channel inlet incorporating a frit element inflow of fluid. The complicating influences of hydrodynamic lift forces and diffusion can therefore be ignored. Numerical simulations of the flow inside the channel were performed using the Fluent V4.0 Navier–Stokes solver. Three-dimensional models were constructed to examine the effect of the geometry of the system on the relaxation efficiency and sample zone broadening. Particle trajectories were computed by integration of the hydrodynamic force balance on a particle as it is driven through the system by the flow of fluid. Two commonly used geometries for the frit element were examined. In one, the frit extends a short distance beyond the triangular channel end-piece, and in the other the frit is entirely contained within the end-piece. These numerical simulations were carried out in order to improve our understanding of the flow patterns within frit-inlet systems, which may in turn lead to improvements in the design and operation of these systems.

2. Principle of the simulation

The laminar flow inside the triangular end-piece of the channel and the flow percolation through the frit element were computed in three-dimensions using the Navier–Stokes solver Fluent, based on a finite-volume technique. The geometry of the computational domain is shown in Fig. 1. A discretization of 50 400 cells was used to compute the flow, and hence, the trajectories of particles carried by the flow. The boundary condition at the entrance of the computational domain ($z=z_s$) was a uniform inflowing velocity $U_s=(0, 0, u_{zs})$. For the inlet flow to be established before entering the triangular channel end-piece, a short square duct was included in the model ahead of the end-piece, in line with the channel (see Fig. 1). The leading edge of the frit element (at z_1) was placed at a sufficient distance from the entry of the duct to the end-piece (at z_0) to ensure a fully developed flow (i.e., a parabolic flow profile) before the merging of the streams commenced. A uniform carrier fluid flux was prescribed at the top surface of the frit element. The pressure loss through the porous material Δp, was related to the mean filter velocity, or equivalently the flux density q, according to Darcy's law (inertia-free) given by:

$$q = -\frac{K_0}{\mu}\frac{\Delta p}{w_f} \tag{3}$$

where w_f is the thickness of the frit element, K_0 is the specific permeability of the frit material, and μ the dynamic viscosity of the fluid. The specific permeability was assumed to be uniform and identical in each component direction (X, Y, Z). To analyze the efficiency of the hydrodynamic relaxation process, the trajectories of a set of micron-size particles were computed by integration of the force balance on the particles without consideration of the effect of a sedimentation field (i.e., for the simulations the density of the particles ρ_p was set equal to that of the fluid ρ) or an outflow through a permeable accumulation wall (as found in the technique of flow FFF). This effectively isolated the hydrodynamic relaxation process from the complicating influence of a simultaneous field-driven relaxation. In practice,

the rate of field-driven relaxation may be assumed to be small in comparison to the rate of hydrodynamic relaxation. If this was not the case there would be no need for hydrodynamic relaxation. The particle size was assumed to be large enough that diffusional transport was negligible, and sufficiently small that hydrodynamic lift forces could also be ignored. Each particle trajectory was computed from the plane $z=z_0$, located just at the entry of the duct to the end-piece (see Fig. 1). The particle velocity $U_0=(u_{x0}, u_{y0}, u_{z0})$ at the starting point $P_0=(x_0, y_0, z_0)$ was assumed to be equal to the local flow velocity, because the sample particles are driven only by the flow inside the channel. The sample was assumed to be introduced at very low concentration so that particle–particle interactions could be neglected in the simulation.

In practice, the geometry of the entry port differs in some aspects from that described above. The sample-inlet flow generally enters via a thin tube of circular cross section through the depletion wall (or, in some cases, the accumulation wall). The geometric characteristics of the entry port (i.e., its size, shape, etc.) and its location inside the triangular end-piece will influence the initial distribution of the particle cloud, and hence the degree of band-broadening. The exact modelling of the entry port is considerably more difficult to achieve than the in-line square duct model assumed here. In this study, we limit our consideration to the simple analysis of the hydrodynamic relaxation process and its effect on the band-broadening. The simplified model serves this purpose, and further complications to the geometry are therefore unnecessary.

The different particle trajectories (i.e., their path and local velocity) were calculated as a function of starting position P_0. Their transit times t (from z_0 to z_3) and the transit time spread $\Delta t=t(\max)-t(\min)$ were predicted without any assumption concerning the initial distribution of particles. The standard deviation in transit time σ_t was calculated for an assumed uniform distribution of particles at the injection point z_0 (although a condition of $x_0/w>0.2$ was imposed, as explained below). Both Δt and σ_t give some indications about the band-broadening effect.

A particle contacting a wall of the channel was assumed to rebound with a coefficient of restitution of unity. In practice, the wall boundary conditions and the particle–wall interactions are more complicated. In the case of steric mode FFF, when the particle approaches the accumulation wall, the force balance is dominated by the so-called near-wall hydrodynamic lift force [6]. Under a complex mechanism, the particle stabilizes at an equilibrium position across the flow profile, and no contact occurs between the particle and the wall. To avoid these complications and to limit particle–wall interactions, the analysis was not carried out for particles starting from initial positions relatively close to the accumulation wall (i.e., for $x_0/w<0.2$). Consequently our model yields values for Δt and σ_t that underestimate the true values.

3. Results and discussion

The frit efficiency and the inlet band-broadening effect were analyzed for two different designs of frit inlet. The first corresponds to the experimental system described by Giddings [11], ($w=220$ μm, $w_f=3$ mm, $b=20$ mm, $z_1=2$ mm, $z_2=34$ mm, $z_3=40$ mm, $L_e=24$ mm) as shown in Fig. 1. The second has a shorter frit element, entirely included in the triangular end-piece of the channel ($w=220$ μm, $w_f=3$ mm, $b=20$ mm, $z_1=2$ mm, $z_2=20$ mm, $z_3=40$ mm, $L_e=24$ mm). Particle trajectories were determined for a sample inlet flow-rate $\dot{V}_s=0.4$ ml/min, and a percolation flow-rate through the frit element $\dot{V}_f=10\ \dot{V}_s$, so that channel flow-rate $\dot{V}=\dot{V}_s+\dot{V}_f=4.4$ ml/min. The carrier fluid was assumed to be water with dynamic viscosity 0.001 N s m^{-2} and density 1×10^3 kg m^{-3}. A permeability of 2×10^{-15} m^2 was determined for the frit material by experiment and this value assumed for the simulations.

The pattern of streamlines in the Y–Z plane is very similar to that for ideal Newtonian flow through a simple triangular end-piece without frit inflow predicted using an approach based on a Schwarz–Christoffel transformation [17] (see Fig. 2). A set of trajectories for particles initially located at $x_0/w=0.5$ and various y_0 are shown in Fig. 2. The relationship between the initial y_0 of 3, 24, 51, 78, and 105 μm (just within the square inlet duct) and

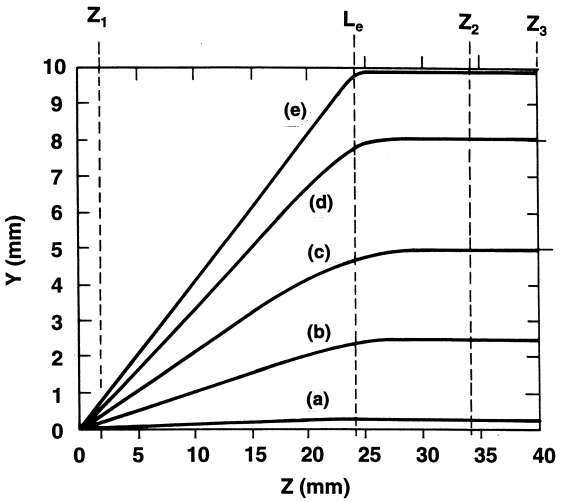

Fig. 2. Particle trajectories in the Y–Z plane of the triangular end-piece with frit design 1. At the entry port ($z=z_0$) the channel breadth is equal to 220 μm. Starting positions correspond to: (a) $y_0=3$ μm, (b) $y_0=24$ μm, (c) $y_0=51$ μm, (d) $y_0=78$ μm, (e) $y_0=105$ μm (y_0 measured from the center line). All the particles start at the same elevation $x_0/w=0.5$.

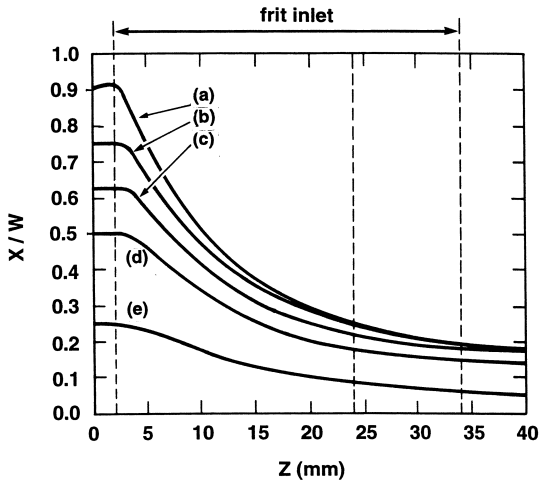

Fig. 3. Particle trajectories in the X–Z plane close to channel center line ($y_0=3$ μm) for frit design 1 with the different initial elevations: (a) $x_0/w=0.91$, (b) $x_0/w=0.75$, (c) $x_0/w=0.625$, (d) $x_0/w=0.5$, (e) $x_0/w=0.25$.

the final y_f of approximately 0.3, 2.5, 5.0, 8.0, and 9.9 mm, respectively, in the channel at $z_3=40$ mm is determined by the transformation of the flow profile closely following the entry of fluid into the end-piece. The fully developed flow in the square duct must very rapidly assume a radial flow pattern (with edge perturbations) in the Y–Z plane and a parabolic profile across the thickness. The higher flow in the central region of the inlet duct contributes a relatively wide radial spread of flow through the end-piece, while the lower flow entering close to the edges of the duct is spread to a lesser degree. The result is that the particle initially located at $y_0=105$ μm in the duct (or 5 μm from the duct wall) remains close to the edge of the end-piece as it is driven forwards by the flow. The particle is predicted to be only approximately 100 μm from the edge of the channel after completing its passage through the end-piece. This proximity to the channel edge wall has a significant effect on the particle trajectory as we shall see below.

While the particles are being distributed across the breadth of the channel they are driven toward the accumulation wall by the complementary frit flow. Fig. 3 shows the predicted trajectories of particles across the channel thickness as they pass through the end-piece close to the center-line of the channel. Initial transverse positions corresponding to x_0/w of (a) 0.91, (b) 0.75, (c) 0.625, (d) 0.5, and (e) 0.25 are represented. A simple model that assumes purely radial flow from a point source in the Y–Z plane with uniform supplementary frit flow for all path directions would predict final transverse positions x_f/w of 0.184, 0.170, 0.152, 0.129 and 0.070, respectively. The simulation deviates slightly in its predictions from this naive model. For example, trajectory (e) falls from x_0/w of 0.25 to x_f/w close to 0.05. This again is almost certainly a result of the complicated transformation of flow profile close to the inlet of the channel.

Fig. 4 shows the predicted trajectories of particles across the channel thickness as they follow different paths across the breadth of the end-piece and channel. Trajectories (a), (b), (c), and (d) correspond to initial y_0 of 3, 51, 78, and 105 μm, respectively, and all originate at x_0/w of 0.91. In this case, the simple model of radial flow with uniform complementary frit flow would predict a final transverse position x_f/w of 0.184 for all particle trajectories starting at $x_0/w=0.91$. The trajectories shown in Fig. 4 differ in their x_f/w positions, and in their respective variations of x/w with z beneath the frit. Consider

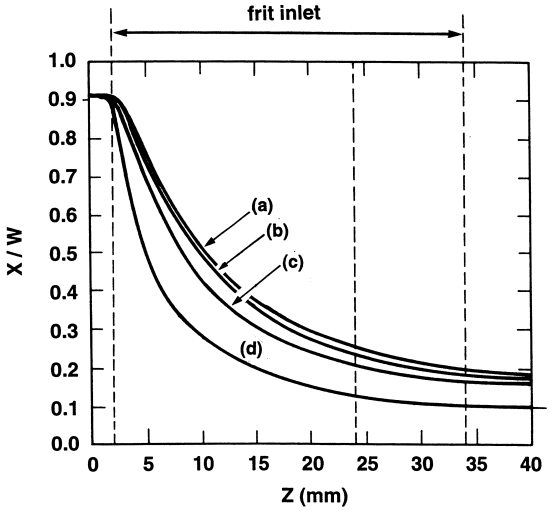

Fig. 4. Particle trajectories in the X–Z plane for frit design 1 for the different lateral starting positions: (a) $y_0=3$ μm, (b) $y_0=51$ μm, (c) $y_0=78$ μm, (d) $y_0=105$ μm. Initial elevation in the channel thickness $x_0/w=0.91$ for all trajectories.

trajectories (a), (b), and (c) which follow different radial paths through the end-piece. We expect their radial velocities to vary through the end-piece (due to the varying cross sectional area and the changing volumetric flow-rate), but their radial velocities should vary in parallel and remain very similar. The trajectories are not plotted in terms of x/w versus radial distance from the inlet however. The projection of each trajectory in the z-direction accounts for the initial difference in their slopes when plotted as x/w versus z. Also the path length beneath the frit element is longer for trajectory (b) than for trajectory (a), and longer still for trajectory (c). The slightly higher volumetric frit inflow along the path of a longer trajectory would result in a greater displacement toward the accumulation wall. This effect accounts for the slight variation of x_f/w for trajectories (a), (b), and (c). The displacement of the particle following trajectory (d) is much greater however. Certainly a part of the increased displacement is attributable to the mechanism just considered, but the majority of the excess displacement is attributable to a different mechanism. Trajectory (d) follows a path close to the edge wall of the end-piece and channel. The particle is carried through the region where fluid velocity is influenced by the no-slip boundary condition at the edge wall (see Refs. [18,19]). This region extends into the channel a distance comparable to the channel thickness (220 μm in this case). The particle is initially located just 5 μm from the end-piece edge wall, and is predicted to reach a distance of approximately 100 μm at $z_3=40$ mm, as mentioned above. Compared to particles following other paths, it is expected to be strongly retarded in its velocity near the inlet, and less so as it is carried through the end-piece. The great difference in the initial slopes of trajectories (c) and (d) plotted as x/w versus z in Fig. 4 is principally due the reduced velocity dz/dt for trajectory (d), and to a small extent their differing radial directions (as discussed above in the comparison of trajectories (a), (b), and (c)). The transverse velocity dx/dt may also be expected to be influenced to some extent by the proximity of the edge wall (see discussion with respect to Fig. 5 below). The inflow is via a frit, and the transverse path length is relatively short, too short to obtain a fully developed transverse flow. The result is that a particle following trajectory (d) spends more time beneath the frit and is displaced toward the accumulation wall to a greater extent than those following trajectories (a), (b), and (c), as shown in Fig. 4.

The frit-inlet band-broadening is influenced by (1) the differences between particle velocities following the various trajectories (velocities vary along each trajectory and differ between trajectories), and to a

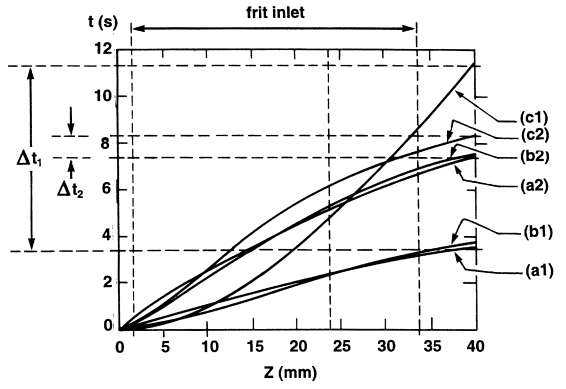

Fig. 5. Plots of transit time versus particle position z with frit design 1. Trajectories correspond to: (a1) $x_0/w=0.91$, (b1) $x_0/w=0.5$, (c1) $x_0/w=0.25$ for $y_0=3$ μm; and (a2) $x_0/w=0.91$, (b2) $x_0/w=0.5$, (c2) $x_0/w=0.25$ for $y_0=105$ μm.

lesser extent (2) the differences in the lengths of the particle trajectories. We can gain some qualitative information concerning the band-broadening by examining the elapsed time of migration as a function of z position for a set of particle trajectories such as those shown in Fig. 5. Curves (a1), (b1), and (c1) correspond to trajectories close to the channel center line ($y_0 = 3$ μm) for initial x_0/w of 0.91, 0.5, and 0.25, respectively. Curves (a2), (b2), and (c2) correspond to trajectories close to the channel edge ($y_0 =$ 105 μm), again for initial x_0/w of 0.91, 0.5 and 0.25, respectively. Curves (a1) and (a2) therefore correspond to trajectories (a) and (b) of Fig. 4, and curves (b1) and (c1) correspond to trajectories (d) and (e) of Fig. 3. The results for (a2), (b2), and (c2) are expected to be strongly influenced by edge effects as discussed previously. This may be deduced from the initial slopes dt/dz of the curves. The greater slopes for (a2), (b2) and (c2) as compared to (a1), (b1) and (c1) indicate a much lower initial velocity dz/dt. The difference is much greater than can be explained by projection of velocity along the Z axis for the different radial directions of the respective trajectories. A factor of, at most, only $1/(\cos 22.6°)$, or 1.083, is attributable to this effect.

Across most of the end-piece and channel breadth, particles initially located at $x_0/w = 0.91$, 0.5, and 0.25 are expected to quite closely follow the curves (a1), (b1), and (c1), respectively. The transit times would be expected to increase with increasing deviation of a trajectory from the center line of the channel. This would be due to (1) the greater path length of these trajectories, and (2) the tendency for these particles to be driven closer to the accumulation wall and therefore into slower stream velocities (as discussed in relation to Fig. 4). The slightly higher final slopes dt/dz (and therefore slightly lower final velocities dz/dt) for (a2) and (b2), compared to (a1) and (b1), are in agreement with the latter effect, although there may also be a small contribution to this difference due to edge effects. We note that curve (c2) indicates a much higher final velocity for this trajectory than that for (c1). This suggests that close to the edge of the end-piece the frit flow is not so effective at driving particles toward the accumulation wall.

Consider curves (a1), (b1) and (c1) of Fig. 5 once more. Particles corresponding to (a1) and (b1) are predicted to be carried to $z = 40$ mm in less than 4 s for the assumed flow regime, while a particle corresponding to (c1) is predicted to take more than 11 s to reach the same z position. This is simply because particles corresponding to (a1) and (b1) are carried through the fastest flowing stream velocities close to the midpoint of the channel thickness, and that corresponding to (c1) is immediately carried away from these fast stream velocities on entering the end-piece and into the slower stream velocities closer to the accumulation wall. The Δt_1 indicated in Fig. 5 shows the spread in transit time through the end-piece for these three trajectories. The interval Δt_2 corresponds to the spread for the corresponding trajectories near the edge wall. It is seen that $\Delta t_2 < \Delta t_1$, but this is a result of the edge effects as discussed above, and this behaviour will apply to only the relatively small population of particles occupying the regions close to each edge wall.

Finally, we shall consider the results obtained for the two different frit element lengths. Fig. 6 shows the trajectories close to the channel center line predicted for the two frit designs for particles initially located at $x_0/w = 0.91$. Curves (a) and (b) correspond to the longer frit element 1 and the

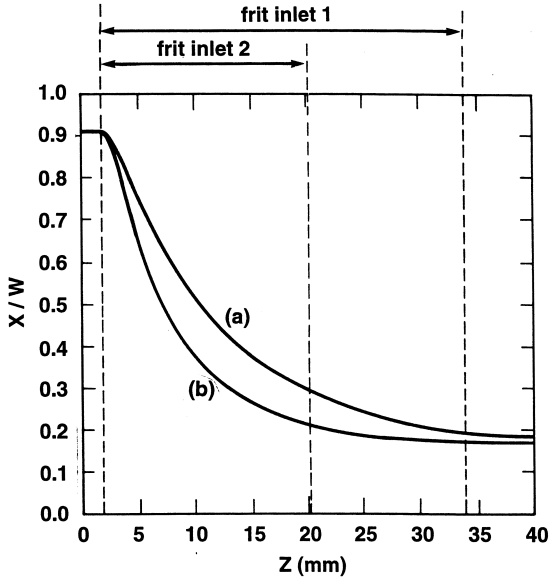

Fig. 6. Influence of the length of the frit element on particle trajectory in X–Z plane for $x_0/w = 0.91$ and $y_0 = 3$ μm: (a) longer frit element 1; (b) shorter frit element 2.

shorter frit element 2, respectively. The volumetric flow regimes are identical, with $\dot{V}_s = 0.4$ ml/min and $\dot{V}_f = 10\ \dot{V}_s$ as before. Considering the limitations of the finite discretizations, the final x/w for the two trajectories are indistinguishable. We note that there is a continuation of the particle approach to the accumulation wall following the shorter frit 2. The simulations were carried out in the absence of an assumed transverse field and this continued approach cannot therefore be attributed to the effects of a field. The explanation must lie in the final approach to fully developed flow conditions that takes place over a short distance downstream of the shorter frit. In the case of the longer frit element, the frit flow enters the channel at a lower velocity and the departure from fully developed channel flow at the downstream edge of the frit element may be expected to be smaller.

Fig. 7 shows the curves of elapsed time versus distance z from the inlet for trajectories close to the channel center line. Curves (a1), (b1), and (c1) correspond to the longer frit 1 with $x_0/w = 0.91$, 0.5 and 0.25, respectively, and curves (a2), (b2), and (c2) correspond to the shorter frit 2 with the same x_0/w. Particles following trajectories corresponding to curves (a1) and (a2) are predicted to be carried most quickly through the computational domain. This is because they traverse the full region of fast flowing streamlines around the central region of the channel thickness. The trajectory corresponding to (a2) has a shorter transit time than that corresponding to (a1) because the complementary frit flow enters the channel before the full channel breadth is attained. For the shorter frit element the mean flow velocity must therefore be higher through the remainder of the channel end-piece and the first 10 mm of the channel. It is the increased flow velocity through the remainder of the end-piece which is of most significance, because the reduced breadth here amplifies the differences in the mean velocities. For the limited range of x_0/w, the predictions suggest a slightly reduced Δt for the longer frit 1. However this does not mean that for an operational system employing a transverse field a longer frit element is beneficial. For example, the steeper final slope dt/dz for (b2) compared to that for (b1) indicates that with frit 2 the particles initially located at $x_0/w = 0.5$ are driven into slower stream velocities and are therefore more relaxed.

To study the influence of the frit element length on band-broadening, the predicted distributions of particle transit times across the computational domain were determined. For each of the two frit designs, 400 particle trajectories were determined and their transit times calculated. The cloud of particles was assumed to be uniformly distributed at the inlet $z = z_0$. The number of particles N exiting the computational domain within consecutive 0.5 second intervals is plotted in Fig. 8 in the form of a histogram for each of the two designs. Histograms (a) and (b) correspond to the longer frit element 1 and the

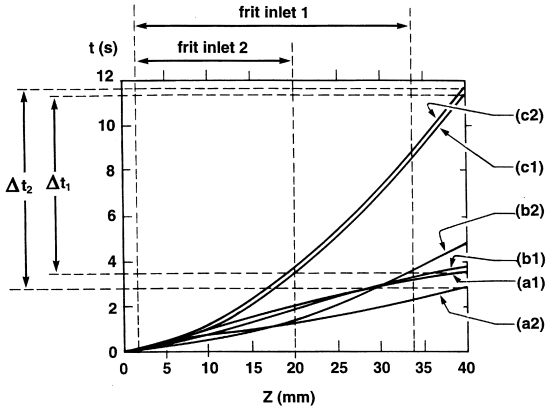

Fig. 7. Influence of frit element length on transit times t. All trajectories for $y_0 = 3$ μm. Longer frit element 1: (a1) $x_0/w = 0.91$, (b1) $x_0/w = 0.5$, (c1) $x_0/w = 0.25$. Shorter frit element 2: (a2) $x_0/w = 0.91$, (b2) $x_0/w = 0.5$, (c2) $x_0/w = 0.25$.

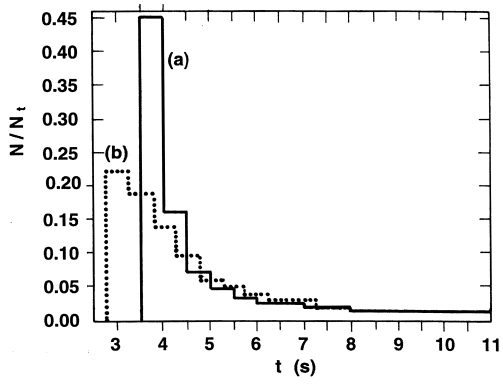

Fig. 8. Relative number of particles N/N_t exiting computational domain versus transit time t. The sampling was performed for consecutive 0.5 s intervals for (a) longer frit element 1; (b) shorter frit element 2.

shorter frit element 2, respectively. In both cases the histograms indicate a sharp front and extended tail for the distributions in transit time. If it had been possible to include trajectories originating at $x_0/w<$ 0.2 the tails would have been even more extended. The histograms suggest that band-broadening is slightly greater in the case of the shorter frit element 2. A quantitative measure of the band-broadening effect is given by the standard deviation σ_t in transit time across the computational domain, as given by:

$$\sigma_t = \sqrt{\frac{1}{N_t}\sum_{1}^{N_t}(t-\bar{t})^2} \quad (4)$$

where $\bar{t}=1/N_t\ \Sigma_1^{N_t}t$ is the mean transit time and N_t is the number of trajectories considered. It was found that $\bar{t}_1=4.5$ s and $\sigma_{t1}=1.09$ s for the longer frit element 1, and $\bar{t}_2=4.2$ s and $\sigma_{t2}=1.25$ s for the shorter frit element 2. (Material in the extended tails corresponding to $t>7.5$ s was neglected in these calculations). The mean transit times are consistent with the transit times of (b1) and (b2) of Fig. 7. The mean transit times are a little longer than for the two trajectories (b1) and (b2), both of which commence at $x_0/w=0.5$ and follow paths close to the channel center line. The mean times represent the full range of paths across the breadth of the end-piece and channel, and so are expected to be a little longer. We should be cautious in concluding that a longer frit element is generally beneficial however. When the transit time distributions are convoluted with the much greater degree of band-broadening that occurs along the length of the channel, the material in the extended tails cannot be neglected.

The band-broadening associated with hydrodynamic relaxation does appear to be a relatively small effect for the flow regime considered, and only likely to be significant under very high resolution conditions. The effect would be most noticeable for relatively narrow peaks eluted within a few channel void volumes, such as may be obtained with flow/hyperlayer FFF. An example of such a high resolution fractogram of a mixture of polystyrene particle standards is shown in Fig. 9 of Ref. [20]. A channel flow-rate of 4.98 ml/min was used for this example, which is just a little higher than that considered for our simulations (4.4 ml/min), and this resulted in a void time of 15.5 s assuming a geometrical channel volume of 1.29 ml. The narrowest peaks exhibit an apparent efficiency of around 600 plates. The 10 μm standard elutes in about 53 s with a width at half-height close to 5 s, corresponding to a σ_t of just over 2 s. For this peak, the additional contribution to band-broadening predicted for frit-inlet relaxation would be significant. In terms of plate height, the 10-μm peak exhibits an apparent plate height of 0.043 cm for the channel length of 25.8 cm; the frit inlet would contribute an additional 0.011 cm to plate height (assuming frit design 2, with $\sigma_{t2}=1.1$ s to compensate for the higher channel flow-rate). The effect is less significant for more retained components. The 7-μm peak exhibits an apparent plate height of 0.041 cm (retention time $t_r=88$ s, $\sigma_t=3.5$ s) and in this case the frit inlet would contribute only an additional 0.004 cm. The significance of the frit-inlet contribution to plate height decreases rapidly for more retained components.

It must be emphasized that these predictions are based on a number of assumptions and approximations: (1) It was assumed that the initial distribution of material across the channel thickness is uniform. (2) A, perhaps important, portion of the sample corresponding to $x_0/w<0.2$ was omitted from the calculations, this being necessary because of computational difficulties stemming from the coarseness of the discretization. (3) The effects of hydrodynamic lift forces, particle-wall and particle–particle interactions were ignored. It follows that the quite significant differences in efficiency between stop-flow and hydrodynamic relaxation that have sometimes been observed (see, for example, Ref. [12]) are probably due to imperfections in the frit-inlet construction. For example, the permeability of the frit element may not be uniform. There could also be some variation in channel thickness beneath the frit element if it is improperly mounted.

4. Conclusion

The usefulness of hydrodynamic relaxation using a frit-inlet system has been demonstrated in earlier work by experiment. The advantages with regard to ease of operation, elimination of the baseline disturbances associated with valve switching, and reduced

tendency for sample adsorption on the accumulation wall are unquestioned. The simulation described in this work of the merging flows within the inlet region of such an FFF channel has revealed its true complexity however. The complexity was shown through the calculated trajectories of particles entrained in the flow. An aspect of the transformation of flow from the inlet duct to the radial flow of the triangular end-piece was shown in the greater radial spread of particles entering close to the center of the inlet duct. For a uniformly permeable frit element, the frit flow is quite uniform over its surface. The length of the path of a trajectory beneath the frit was shown to influence its final transverse position across the channel thickness. The no-slip boundary condition at the edge walls was shown to influence particle motion in both longitudinal and transverse directions in the region of the frit inlet. The variation in transit times of particles passing through the frit inlet is due to variation in the lengths of their trajectories, and variation in velocities between trajectories. Only two frit designs, differing only in their length and placement (i.e., extending beyond, or included within the triangular channel end-piece), were considered. Given the limitations of the simulation, it was not clear if one design would in practice be significantly better than the other.

It is apparent that further work is needed to fully characterize the band-broadening associated with the relaxation process. An improved discretization is required to determine trajectories of particles across the full channel thickness. The inclusion of hydrodynamic lift forces in the model would make comparison with experiment more meaningful. Simulations should also be carried out where the effects of a transverse field are taken into account. It was stated earlier that under practical conditions the rate of field-driven relaxation is likely to be small compared to the rate of hydrodynamic relaxation. However, the determination of the optimum flow-rate ratio $\dot{V}_s/\dot{V}$ via a minimization of the sum $H_r + H_f + H_{di}$ requires a good estimation of the individual contributions. In particular, the prediction of the residual relaxation contribution H_r has, in previous treatments [12], assumed a uniform particle distribution within the sample lamina following hydrodynamic relaxation. For the case of frit-inlet relaxation this may not be the case. A simulation of the complete process would resolve the issue, at least in the case of an ideally constructed system. Ultimately, other parameters such as the frit element shape and the end-piece angle could be considered. The numerical approach is, without doubt, required for the evaluation of such parameters.

Acknowledgements

The authors wish to thank Prof. Paul Schettler of Juniata College, PA for the measurements of frit element permeability, and Prof. Phillip Ligrani of the Department of Mechanical Engineering, University of Utah for providing access to the computing facilities of the CADE Laboratory, University of Utah. One of the authors (PSW) was supported for this work by Public Health Service Grant GM 10851-39 from the National Institutes of Health.

References

[1] J.C. Giddings, Science 260 (1993) 1456–1465.
[2] J.C. Giddings, Sep. Sci. Technol. 19 (1984) 831–847.
[3] J.C. Giddings, Anal. Chem. 67 (1995) 592A–598A.
[4] J.C. Giddings, K.D. Caldwell, in: Physical Methods of Chemistry, Vol. 3B, B.W. Rossiter, J.F. Hamilton, (Eds.), John Wiley and Sons, New York, 1989, Chapter 8, pp. 867–938.
[5] M. Martin, P.S. Williams, in: Theoretical Advancement in Chromatography and Related Separation Techniques, F. Dondi, G. Guiochon (Eds.), NATO ASI Series C: Mathematical and Physical Sciences, Vol. 383, Kluwer Academic Publisher, Dordrecht, The Netherlands, 1992, pp. 513–580.
[6] P.S. Williams, S. Lee, J.C. Giddings, Chem. Eng. Commun. 130 (1994) 143–166.
[7] F.J. Yang, M.N. Myers, J.C. Giddings, Anal. Chem. 49 (1977) 659–662.
[8] M.E. Hovingh, G.E. Thompson, J.C. Giddings, Anal. Chem. 42 (1970) 195–203.
[9] J.C. Giddings, Anal. Chem. 57 (1985) 945–947.
[10] S. Lee, M.N. Myers, J.C. Giddings, Anal. Chem. 61 (1989) 2439–2444.
[11] J.C. Giddings, Anal. Chem. 62 (1990) 2306–2312.
[12] M.-K. Liu, P.S. Williams, M.N. Myers, J.C. Giddings, Anal. Chem. 63 (1991) 2115–2122.
[13] M.-K. Liu, P. Li, J.C. Giddings, Protein Sci. 2 (1993) 1520–1531.
[14] P. Li, M. Hansen, J.C. Giddings, J. Microcol. Sep. 10 (1998) 7–18.

[15] P.S. Williams, S. Levin, T. Lenczycki, J.C. Giddings, Ind. Eng. Chem. Res. 31 (1992) 2172–2181.
[16] J.C. Giddings, M.R. Schure, M.N. Myers, G.R. Velez, Anal. Chem. 56 (1984) 2099–2104.
[17] P.S. Williams, S.B. Giddings, J.C. Giddings, Anal. Chem. 58 (1986) 2397–2403.
[18] J.C. Giddings, M.R. Schure, Chem. Eng. Sci. 42 (1987) 1471–1479.
[19] J. Janca, M. Hoyos, M. Martin, Chromatographia 33 (1992) 284–286.
[20] B.N. Barman, E.R. Ashwood, J.C. Giddings, Anal. Biochem. 212 (1993) 35–42.